Acta Materialia 301 (2025) 121474

Contents lists available at ScienceDirect

Acta Materialia

journal homepage: www.elsevier.com/locate/actamat

Full length article

Unlocking superior fracture resistance in micro-ceramics for architected meta-materials via ALD stress engineering

Wenjuan Cheng [a], Edoardo Rossi [a,e,*], Jens Bauer [b,c], Jose Paolo Martins [d], Raphael Guillemet [d], Laszlo Pethö [f], Johann Michler [f], Marco Sebastiani [a,e]

[a] Università degli Studi Roma Tre, Department of Civil, Computer science and Aeronautical Technologies Engineering, Via Vito Volterra 62, Rome, 00146, Italy
[b] Karlsruhe Institute of Technology, Institute of Nanotechnology, Hermann-von-Helmholtz-Platz 1, Eggenstein-Leopoldshafen, 76344, Germany
[c] Karlsruhe Institute of Technology, Institute for Applied Materials, Kaiserstrasse 12, Karlsruhe, 76131, Germany
[d] THALES Research & Technology, Avenue Augustin Fresnel 1, Palaiseau, 91120, France
[e] Consorzio Interuniversitario Nazionale per la Scienza e Tecnologia dei Materiali (INSTM), Via Giuseppe Giusti 9, Florence, 50121, Italy
[f] Empa, Swiss Federal Laboratories for Materials Science and Technology, Laboratory for Mechanics of Materials and Nanostructures, Feuerwerkerstrasse 39, Thun, 3602, Switzerland

ARTICLE INFO

Keywords:
Atomic layer deposition (ALD)
Architected materials
Crack propagation resistance
Residual stress

ABSTRACT

Micro- and nano-architected metamaterials exhibit remarkable mechanical properties, particularly damage tolerance from the interplay between design and material properties, yet their fracture mechanisms remain poorly understood. Strategies to tailor toughness in response to the anisotropic stress distributions experienced are lacking. Here, we demonstrate a novel approach to enhance the fracture toughness of micro-trusses by up to 165% via interface engineering, leveraging the high surface-to-volume ratios in these materials. We investigate the role of residual stress induced by Atomic Layer Deposition (ALD) on fracture behavior using cohesive-zone finite element simulations and advanced experimental techniques, including pillar-splitting indentation cracking and advanced residual stress measurements. Experiments were conducted on fused silica micro-pillars (fabricated via deep reactive ion etching) and glassy carbon micro-pillars (produced via two-photon polymerization and pyrolysis), coated with ALD Al_2O_3 or ZnO thin films. Our results reveal that median crack geometry combined with tensile residual stress in the coating enhances apparent toughness by inducing beneficial compressive stress in the substrate. Due to differences in crack morphology, Al_2O_3 coatings increase the toughness of fused silica by 165% but reduce that of glassy carbon. This study establishes ALD-induced stress modulation as a powerful tool for optimizing fracture resistance in micro-architected ceramics.

1. Introduction

Micro- and nano-architected metamaterials represent a transformative approach in the design of lightweight, ultra-stiff, and ultra-strong materials. At reduced scales, size effects and enhanced structural control enable unique mechanical and functional behaviors, providing unprecedented opportunities for material optimization in a wide range of applications [1]. For example, glassy carbon (GC) with micro-architected structures fabricated using two-photon lithography followed by pyrolysis achieves strengths up to 3 GPa [2] and approaches theoretical limits of strength and stiffness [3]. Structures such as bending-dominated lattices, honeycomb configurations, bow-tie designs, and hierarchical woven architectures offer precise control over stiffness, strength, energy absorption, and unconventional properties such as negative Poisson's ratios [4–7].

The application of ceramic or metallic films using techniques such as conformal atomic layer deposition (ALD), electroless plating, and magnetron sputtering significantly enhances the mechanical and functional performance of these metamaterials. For example, the integration of metallic thin films, such as Ni alloys or high-entropy alloys via magnetron sputtering, has demonstrated substantial improvements in load-bearing capacity and resilience [8–10]. Compared with other coating techniques, ALD stands out for its exceptional ability to produce films with unparalleled uniformity and atomic-scale thickness control, facilitating precise engineering of material interfaces [11]. For instance, Al_2O_3 films deposited via ALD have been shown to strengthen polymer-based [12] and glassy carbon-based [2] nano- and micro-lattice scaffolds, even with thicknesses of 10–50 nm. Surface roughness,

* Corresponding author at: Università degli Studi Roma Tre, Department of Civil, Computer science and Aeronautical Technologies Engineering, Via Vito Volterra 62, Rome, 00146, Italy.
E-mail address: edoardo.rossi@uniroma3.it (E. Rossi).

https://doi.org/10.1016/j.actamat.2025.121474
Received 1 May 2025; Received in revised form 24 July 2025; Accepted 22 August 2025
Available online 18 September 2025

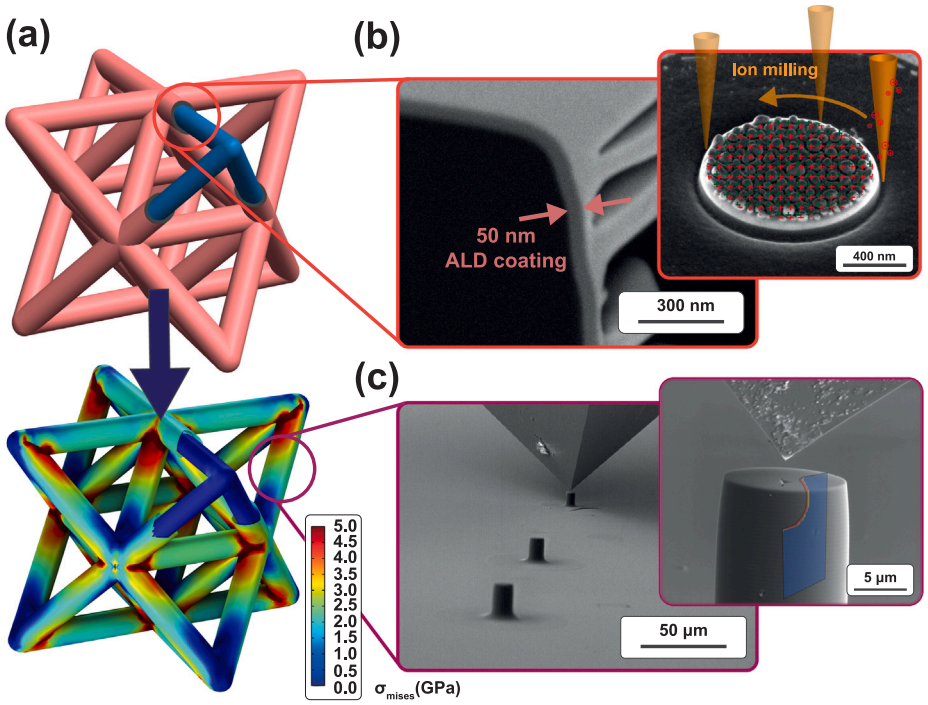

Fig. 1. (a) Illustrative octet-truss unit cell coated with a thin film (top, film in reddish color) and the anisotropic compressive stress distribution (superimposed on the residual stresses from the film) from finite element simulation (bottom); (b) Al_2O_3 ALD coating on glassy carbon and Focused ion beam–digital image correlation method (FIB-DIC) for accurate residual stress measurement; (c) Pillar splitting method with a sharp indenter to evaluate the apparent fracture toughness of coated micro-pillar with the inset cross-section exhibiting crack geometry simulated through cohesive zone finite element model. (For interpretation of the references to color in this figure legend, the reader is referred to the web version of this article.)

flaws, and processing-related imperfections often render GC metamaterials sensitive to environmental conditions such as humidity and temperature fluctuations [13]. The use of coating films as barriers against environmental degradation can substantially improve reliability. However, one universal byproduct of these deposition techniques, particularly ALD and sputtering, is the generation of residual stresses within the film–substrate system. These stresses, often inherent to growth mechanisms and thermal mismatch, can profoundly influence fracture behavior.

Residual stress in thin films has been widely investigated. It is well established that compressive residual stress can enhance the apparent toughness of films by suppressing crack opening and delaying crack propagation, while tensile residual stress often accelerates crack growth and reduces mechanical reliability [14,15]. Most of these investigations focus on the fracture behavior of the film itself, often considering relatively thick coatings or planar geometries. Much less attention has been given to how ultrathin films, on the order of tens of nanometers, modify the fracture resistance of the underlying substrate, especially in microscale architectures where surface effects are amplified.

The mechanical response of architected materials built from brittle constituents often depends on the behavior of their load-bearing elements. In realistic microarchitectures, failure is not a purely global event but typically initiates locally at regions of elevated stress or geometric imperfections. Recent work by Shaikeea et al. [16] has shown that in ideal elastic–brittle lattices such as the octet-truss, failure strength rather than fracture toughness controls the onset of collapse, due to the absence of damage zones and the discrete nature of load transfer across struts. Their results, which are held in systems where the characteristic strut size is small relative to the critical flaw size, highlight the limitations of continuum fracture mechanics in describing the structural response at the lattice scale. However, in practical implementations of brittle micro-lattices, individual struts often exhibit manufacturing-induced flaws, surface damage, or non-negligible residual stress fields. Under such conditions, local failure may no longer be governed solely by the intrinsic strength of the material but instead becomes sensitive to crack initiation and propagation criteria. Experimental studies have shown that introducing flaws in brittle lattice components can shift the failure mechanism toward a toughness-limited regime, even in nominally strength-dominated architectures [17]. Furthermore, thin-film coatings have been demonstrated to modulate crack resistance in brittle micro-architectures by altering surface stress and fracture behavior [18].

In this work, we investigate how residual stress introduced by conformal ALD coatings affects the apparent fracture toughness of micro-ceramic elements. By isolating individual coated pillars and subjecting them to controlled fracture experiments (Fig. 1), we quantify the influence of interface properties and internal stress fields on crack resistance in fused silica and glassy carbon. These materials, being archetypal brittle systems with process zones much smaller than the feature size, provide a suitable platform for assessing coating-induced modifications in local fracture behavior. The focus is placed on the mechanics of damage initiation in coated struts, which remains relevant to the overall failure evolution in architected materials, even when strength-based metrics ultimately describe the global failure. To achieve this, Plasma-enhanced (PE) and Thermal (TH) Atomic Layer Deposition (ALD) were employed to fabricate Al_2O_3 and ZnO thin films on two types of ceramic substrates—fused silica and glassy carbon micropillars. The details can be seen in Table 1. Special attention was given to the effects of the residual stress state in the deposited thin films on the crack propagation mechanisms. Two main advanced analysis techniques were employed: (i) high-resolution focused ion beam–digital image correlation (FIB-DIC) [19–22], enabling precise residual stress measurements at localized regions, providing a powerful tool for analyzing the stress level in ultra-thin films (Fig. 1b); (ii) pillar splitting [23], which is exhibited in Fig. 1c, to evaluate the apparent fracture toughness of the coated systems in an efficient, geometrically convenient and statistically reliable way. The experimental campaign is crucially accompanied by Cohesive Zone Finite Element Method

Table 1
Overview of micro-pillars fabricated via two different lithographic techniques and ALD coating method. The table details the substrate material, deposited oxide, ALD thickness, and process parameters, including deposition type and temperature.

Microfabrication method	Micro-Pillar material	Coating material	Coating thickness[a] (nm)	ALD process type	Process temperature (° C)
Two-Photon Lithography and Pyrolysis	Glassy Carbon	Al_2O_3	50 (50.9)	Plasma-enhanced	200
		Al_2O_3	50 (50.9)	Thermal	200
		Al_2O_3	50 (44.4)	Thermal	350
Deep Reactive Ion Etching Lithography	fused silica	Al_2O_3	50 (45.7)	Plasma-enhanced	250
		Al_2O_3	50 (50.5)	Thermal	200
		Al_2O_3	50 (53.7)	Thermal	300
		Al_2O_3	100 (96.4)	Thermal	300
		ZnO	50 (55)	Thermal	100

[a] The values inside the parentheses represent the actual coating thickness, which was used for experimental data analysis. For simplicity, the nominal values of 50 and 100 were used in the main text description.

(FEM) simulations offering detailed insights into stress distributions and deformation mechanisms, thereby providing a more comprehensive understanding of the fracture behavior in these systems. By integrating experimental and computational approaches, this work seeks to provide new insights into the role of surface modifications and residual stress in enhancing the mechanical reliability of micro-architected metamaterials, offering guidance for the design of next-generation materials with tailored properties by fine-tuning the interface stress level.

2. Materials & methods

2.1. Description of the finite element model

The primary objective of the finite element simulations is to analyze crack propagation behavior during pillar indentation and to examine how residual stress in the film affects the crack resistance of a ceramic substrate across various crack configurations. Based on this ambition, the commercial package ABAQUS/Standard is used for the cohesive zone finite element simulations [24]. As shown in Fig. 2a, a three-dimensional, six-fold symmetric finite element model with the rigid Berkovich pyramidal indenter tip, characterized by a centerline-to-face angle of 65.3°, was generated because of the symmetric boundary conditions. Crack planes with cohesive elements were positioned perpendicular to the free surface and aligned with the edges of the indenter (Fig. 2a) due to the fact that the cracks are generated along the indenter edges only irrespective of three-sided indenter if the symmetric conditions are maintained [25].

Due to the limitation of the cohesive element model, the crack length had to be at least 10 times greater than the cohesive zone, a micro-pillar with a 150 μm radius and a 300 μm height was used to simulate the uncoated substrate. To replicate experimental conditions, thin films with thicknesses of 3 μm and 6 μm were added to the top and side surfaces of the substrate, corresponding to the real tests with 50 nm and 100 nm films, respectively (R:t = 50:1 and 25:1). Over 30,000 fully integrated elements (C3D6 and C3D8) were employed, with the mesh refined near the contact interface and coating regions to ensure accurate results. The constitutive behavior of the elements was characterized by three key material properties: elastic modulus (E), Poisson's ratio (ν), and yield strength (Y), as summarized in Table 2. The parameter settings follow the previous work of Johanns and Bruns [25,26], which established conditions to induce distinctly different crack geometries during indentation. The substrate, when $E/Y = 9.3$, is expected to create median crack, while $E/Y = 102.77$ will induce Palmqvist crack [25]. The behavior of fused silica which develops median cracks was modeled using the Drucker–Prager Cap plasticity model to account for densification effects, which are typically present for such materials [26]. This modeling approach enables a detailed investigation of how residual stress influences crack propagation under different fracture modes.

Firstly, residual stress was introduced via a predefined temperature and thermal step, allowing control over the temperature difference to replicate experimental conditions (Fig. 2b). Different thermal expansion coefficients were assigned to substrate and film materials to create thermal strain. The simulated stress value (σ_{th}) was approximated using the relationship [27]:

$$\sigma_{\mathrm{th}} = f\left(E_f,\ E_s,\ \nu_s, \nu_f;\ (T_{\mathrm{D}} - T_{\mathrm{M}}),\ (\alpha_f - \alpha_s);\ R/t\right) \tag{1}$$

where E_f is the elastic modulus of the film, E_s is the elastic modulus of the substrate, ν_s is the Poisson's ratio of the substrate, ν_f is the Poisson's ratio of the film, α_f and α_s are the thermal expansion coefficients of the film and substrate, T_{D} and T_{M} are the deposition and room temperatures, which are achieved as predefined temperature and final temperature in thermal step respectively, R/t is the pillar radius versus coating thickness. It is important to note that the residual stress in the actual experiment results not only from the thermal mismatch during cooling but is primarily due to intrinsic stress generated during the film growth, which is more complex. Here, a simplified thermal step was employed to approximate the final residual stress value.

Crack extension in the current simulations was modeled with Abaqus bi-linear traction–separation-based cohesive elements (COH3D8) with zero initial thickness. The debonding initiation was governed by a MAXS criterion, and crack nucleation was defined using a fracture energy parameter. Under the condition of linear elastic fracture mechanics (LEFM), the fracture energy (G_{Ic}) can be related to fracture toughness through:

$$K_{Ic} = \sqrt{\frac{EG_{Ic}}{1-\nu^2}} \tag{2}$$

The values are reported in Table 2. Please note that the G_{Ic} in Equation (2) would be two times of the fracture energy shown in the table since only one COH plane was simulated in the six-fold model. Material properties, loading conditions, and pillar geometry dictated crack growth. Still, it was constrained to remain within the defined crack plane, noting that crack growth in the experiments may have more complex geometries. More details about the cohesive zone model can be checked in previous work [23,25]. The contact between the Berkovich tip and the material surface was modeled as frictionless. The indentation step was performed under displacement control. Crack propagation along the cohesive plane is visualized using the parameter SDEG [28], which represents the stiffness degradation of a cohesive element on a scale from 0 to 1, with 1 indicating complete failure (Fig. 2c). The first load drop represented the material fracture. The value is defined as P_c, the critical instability load. The material-dependent relationship can be described by Eq. (3). The dimensionless constant γ has been determined for various material and tip combinations through cohesive zone finite element modeling [23,29,30]. When testing the same material under different conditions, the ratio of critical loads (P_c)

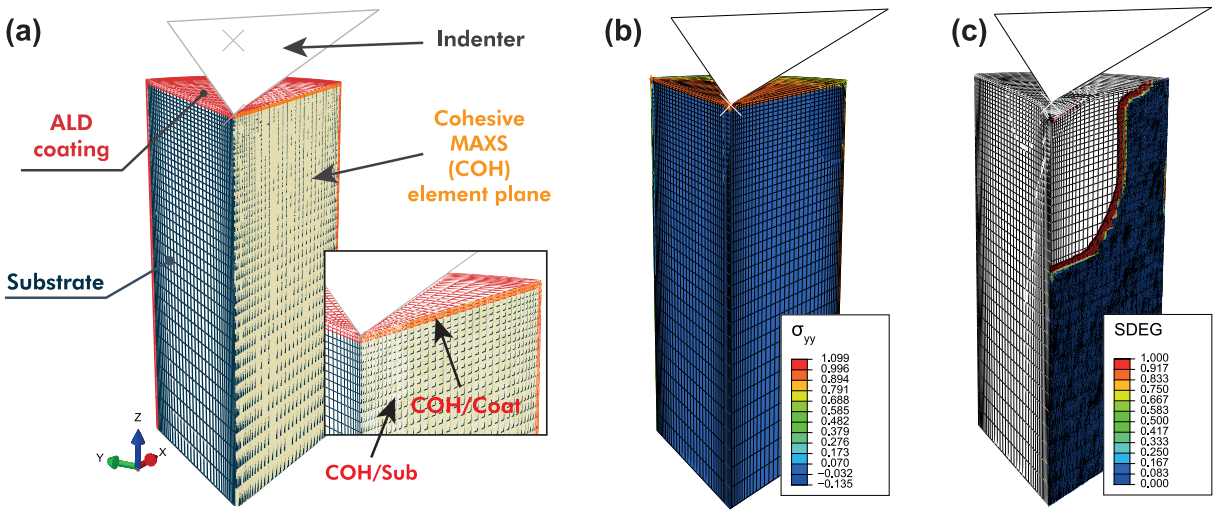

Fig. 2. Finite element model utilized for this work: (a) model characteristics; (b) thermalization step for residual stress equilibrium; (c) indentation and cracking process.

Table 2
Constitutive parameters in finite element simulations.

Materials	Elastic modulus (GPa)	Poisson's ratio (FEM input)	Yield strength (GPa)	Fracture energy (GPa μm)	Fracture toughness (MPa$\sqrt{m}$)
Substrate (median crack)	70	0.18	7.5	0.0125	1.34
Substrate (Palmqvist crack)	185	0.22	1.8	0.01	1.927
Film	180	0.25	5.4	0.00368, 0.02503	1.19, 3.1

directly reflects variations in crack propagation resistance, independent of the calibration constant γ. Given this relationship, the critical load, P_c, will be used as a representative parameter for the apparent fracture toughness of the film–substrate micro-pillar system.

2.2. Micro-pillars fabrication

The fabrication of fused silica micro-pillars followed methods primarily based on the seminal work by Bruns et al. [31], involving lithography-assisted deep reactive ion etching (DRIE). A 500 μm thick, 10 mm diameter fused silica wafer was processed, utilizing a hard aluminum mask due to the low etch selectivity of silica against photoresists. The aluminum mask was patterned using a direct laser writer and an optimized Cl_2/BCl_3 plasma etch. Pillar structures were etched into the silica substrate with a high-rate plasma etch using C_4F_8 and O_2 gases. Subsequent dicing and coating steps protected the pillars, with a diameter of 5.16 μm and a taper angle of 6°. Further details align closely with Bruns et al.'s work.

Pyrolytic carbon micro-pillars were fabricated via two-photon polymerization direct laser writing (TPP-DLW) followed by pyrolysis, as previously described [13]. The TPP-DLW process employed a Photonic Professional GT system (Nanoscribe GmbH) with a 63×1.4 oil objective (Carl Zeiss AG) and a FemtoFiber pro NIR laser (TOPTICA Photonics AG). Polymeric templates were printed from IP-Dip photoresist (Nanoscribe GmbH) on silicon substrates in a layer-by-layer manner, using a galvanometric scanning mode, 19 mW laser power, and 20 000 μm s^{-1} speed. Circular pillars with height-to-diameter ratios of 2 and nominal diameters of 20 μm and 40 μm were constructed with 0.1 μm hatching and 0.2 μm slicing distances. Post-printing, templates were cleaned in propylene glycol monomethyl ether acetate (PGMEA) and isopropanol before critical point drying (Autosamdri-931, Tousimis). Pyrolysis was conducted at 900 °C for 1 h in a vacuum furnace with a ramp rate of 3 °C min^{-1}, causing 70% isotropic shrinkage. Final pillar diameters, measured via SEM (FEI Helios NanoLab™ 600), were 5.3 μm and 11.8 μm.

2.3. ALD coatings

Atomic layer deposition (ALD) was employed to produce conformal ceramic thin coatings on micro-pillars under different process conditions (Table 1) using Beneq TFS200 equipment. Al_2O_3 thin films were deposited using TriMethylAluminium (TMA) as the precursor with O_2 as the oxidant, while ZnO films were deposited using Diethylzinc (DEZ) with H_2O as the oxidant. Fused silica micro-pillars were coated with Al_2O_3 using plasma-enhanced ALD at 250 °C with a biasing configuration (up to 300 W at 13.56 MHz) applied in the plasma module between the source and a grid. No bias was applied to the substrate to prevent coating damage from accelerated species. Additionally, thermal ALD was performed at 200 °C and 300 °C for Al_2O_3 deposition. ZnO films were deposited on fused silica micro-pillars using thermal ALD at 100 °C. To ensure consistency in mechanical property measurements of the thin films, flat silicon wafers (1.2 cm × 4 cm × 0.04 cm) were coated under the same conditions as the fused silica micro-pillars. For glassy carbon micro-pillars, Al_2O_3 coatings were deposited using plasma-enhanced ALD at 200 °C, along with thermal ALD at 200 °C and 350 °C. The targeted film thicknesses were 50 nm or 100 nm for Al_2O_3 and 50 nm for ZnO, depending on the deposition conditions. All thicknesses were confirmed by ellipsometry.

2.4. Nanoindentation testing

Nanoindentation tests were performed under ambient conditions using a G200 (KLA Instruments) system and an iNano (KLA Instruments) system. For all Continuous Stiffness Measurement (CSM) and pillar splitting tests on GC micro-pillars, a Berkovich tip was employed, while a cube corner diamond tip was used for pillar splitting tests on fused silica micro-pillars to minimize the densification effects associated with a blunt tip. Machine compliance and the indenter area function were calibrated on a fused silica reference sample before and after each test, following the procedure outlined by Oliver and Pharr [32].

The mechanical properties of the ALD coatings were characterized by nanoindentation on coated silicon wafers using the continuous

stiffness measurement (CSM) mode. Indentation tests were performed using the iNano system at a constant strain rate of $0.2\,s^{-1}$, with a maximum penetration depth of 100 nm. For each coating, a 4 × 6 array of indents was performed. After excluding outliers due to surface effects or shallow-depth instability, at least 16 valid measurements were used to extract the elastic modulus and hardness. The elastic modulus was extracted using the Doerner–Nix model [33], while the film hardness was corrected for substrate effects using the Korsunsky model [34], as described in the Supporting Information. A Poisson's ratio of 0.26 was assumed for the coatings [35]. To enable accurate application of these models, the mechanical properties of the bare silicon substrate were independently measured. Nanoindentation was performed on uncoated silicon wafers using the same instrument and strain rate, with a maximum depth of500 nm and a 4 × 4 indentation array. A minimum of 12 valid indentations was retained to determine the substrate's modulus and hardness, which were then used as input parameters in the composite analysis of the coated films. For fused silica, indentation was performed on uncoated substrate regions prior to film deposition using the G200 nanoindenter, at a strain rate of $0.05\,s^{-1}$ and a depth of 500 nm, also in a 4 × 4 array with at least 12 valid data points. The mechanical properties of glassy carbon were taken from prior work by the authors [13] and the Poisson's ratio of 0.17 was used from reported value [36].

The crack propagation resistance of micro-pillars with various coatings was evaluated through pillar-splitting experiments. This technique involved applying an indentation load to the pillars until fracture occurred, eliminating the need for post-test crack length measurements [23,29,30]. To ensure consistency in the splitting tests, a brand-new cube corner tip (MicroStar Technologies, nominal radius ≤20 nm) was used. Tip sharpness was regularly monitored, and the area function recalibrated to confirm stability over the entire test campaign. This minimizes the influence of tip blunting on crack initiation loads, as discussed in previous studies [28,37]. As outlined in the FEM section, apparent fracture toughness (K_c) was calculated using the relationship provided in Eq. (3). Nanoindentation pillar splitting tests were conducted on ALD-coated GC and fused silica micro-pillars at a constant strain rate of $0.05\,s^{-1}$ to assess their apparent fracture toughness. The surface roughness of both fused silica and pyrolytic glassy carbon pillars is in the nanometer range, and the conformal ALD coating further reduces surface asperities. Given that the coating thickness and the estimated process zone exceed the roughness scale by at least one order of magnitude, surface roughness is not expected to influence the measured fracture response. Uncoated GC and fused silica micro-pillars were also tested as reference samples, with uncoated diameters of 5.3 μm and 5.16 μm, respectively. The specific calibration coefficient (γ) for the materials was determined through polynomial interpolation of the γ versus E/H ratio function, as established in previous work by the authors [23]. To ensure accuracy in tip positioning [37], only experiments with indenter tips precisely centered on the pillar surface, within 0.5 μm, were considered. The centering was verified through post-experiment scanning electron microscopy (SEM) imaging of residual marks on the substrate.

2.5. Residual stress measurement

Residual stress measurements were conducted on 12 μm GC micro-pillars and the unetched zone of fused silica wafer using the Helios 5 CX system (Thermo Fisher Scientific). The ring-core FIB-DIC procedure developed by the authors in their prior works [19–22] was utilized after ALD coating process. Tests were also performed on uncoated GC samples to establish a baseline for comparison. Several modifications to the published method were implemented to enhance both in-depth and lateral resolution, enabling stress measurements in thin films with an average thickness of 50 nm.

For all cases studied, surface preparation involved the deposition of an ultra-thin sputter-coated gold layer using a 15 μA current for 20 s to enhance the DIC analysis. The gold layer was subsequently irradiated at low ion currents to achieve dewetting, as detailed by Winiarski [38], utilizing a current of 1.5 pA at 30 kV. Incremental material removal in the ring-core geometry was performed via a semi-automated procedure, ensuring precision and repeatability.

This modified method provides high sensitivity for stress measurements in the normalized depth range of $h/D = 0.015 - 2$ [21,22]. To accommodate the film thickness, an annular trench with an inner diameter of 1 μm for GC samples and 0.7 μm for fused silica samples was employed. Each milling step typically achieved a depth of approximately 2 nm, except for the 100 nm coated samples where a milling depth of 4 nm per step was used to reduce the total number of milling steps required. These milling depths were achieved using a low ion milling current and, through precise calibration of milling depth versus ion dose, explicitly performed for each material via cross-sectional measurements of the milled geometries. Maintaining a consistent milling rate throughout the process ensured uniform partial depths after each incremental material removal. A total of 30 milling steps were utilized, corresponding to the film thickness and enabling evaluation of the residual stress depth profile from the surface to the substrate interface.

During the process, five high-resolution SEM micrographs were captured: five before testing and five after each material removal increment. These images were acquired under consistent contrast conditions, using an acceleration voltage of 2 kV, a beam current of 43 pA, and in immersion mode. Each image was integrated over 32 frames at a dwell time of 100 ns per frame. Cross-sectional depth measurements were performed on SEM high-resolution images of the lateral surfaces of the milled geometries to verify the final depth. Following image acquisition, a MATLAB-based digital image correlation (DIC) routine was used to track the incremental strain evolution by comparing each milled-step image to the initial, unprocessed surface. The obtained strain distribution was then utilized to reconstruct the residual stress profile based on the inverse problem approach of the FIB-DIC method, as detailed in Supporting information.

3. Results

3.1. Finite element simulation of film stress effect on crack propagation during pillar splitting

The study focuses on the relative changes of crack propagation resistance in micro-pillars after adding films with various stress levels. Given the specific materials and indenter geometry used, the apparent fracture toughness is associated with the critical instability load, P_c, occurring during sharp nanoindentation of a micro-pillar, through the relationship [23]:

$$K_c = \gamma \frac{P_c}{R^{3/2}} \tag{3}$$

where γ is a dimensionless coefficient, ultimately derived from cohesive-zone simulations, that depends on the material's elastic modulus-to-hardness ratio, Poisson's ratio, and the geometry of the indenter tip. R is the radius of the pillar. Given this, the same γ value could be used for the simulations with various film stress levels. To quantify the variation in splitting load (φ), which serves as an indicator of relative changes in crack propagation resistance, the following expression is used:

$$\varphi = ((P_c - P_{\text{cref}})/P_{\text{cref}}) \tag{4}$$

where P_{cref} represents the critical load of the uncoated substrate pillar simulation. This approach aligns with experimental conditions, where uncoated samples serve as the reference. To understand the basic mechanisms, FEM simulations allow for the investigation of substrates with films that have no residual stress, isolating the influence of the film's mechanical properties. In practice, films with predefined residual stress states are applied to the substrate following the ALD process. This highlights the advantage of using simulations to systematically analyze the impact of film stress and mechanical properties on crack resistance.

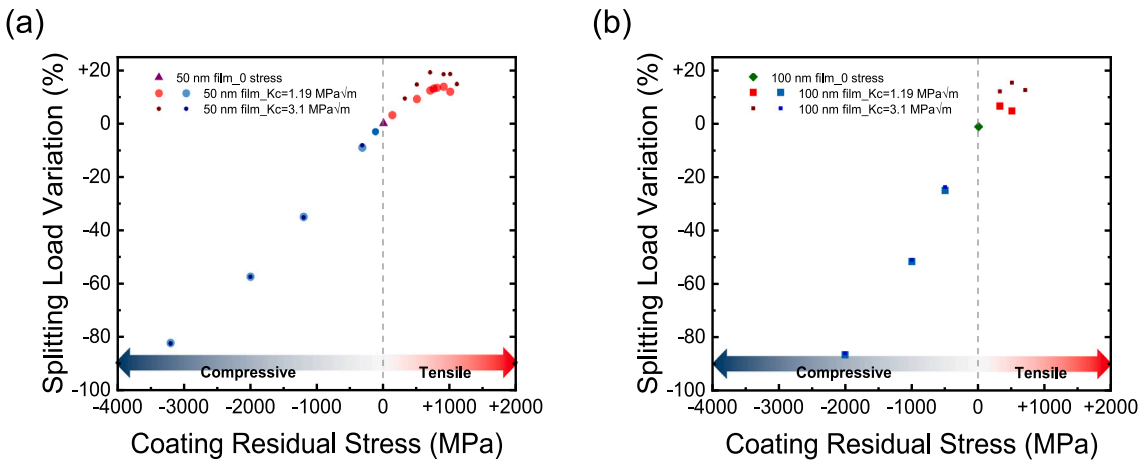

Fig. 3. The splitting load variation of the coated system with (a) 50 nm and (b) 100 nm ALD film on the ceramic substrate which develops median cracks as a function of the film residual stress.

3.1.1. Median crack geometry

The median mode crack propagation behavior can be observed in more detail in the supplementary video (Movie S1), where the crack originated beneath the contact area with the indenter and propagate vertically. Fig. 3 shows how the thin film affects the apparent fracture toughness of the coated pillars. Since median crack propagation is predominantly governed by the substrate's bulk properties, the addition of coating with zero stress has a limited effect (Figure S1). Specifically, 50 nm and 100 nm coatings with zero residual stress show minimal impact on the fracture resistance of the coated pillars, with the φ value varying within ±2%. Compressive residual stress leads to a reduction in critical load, showing a clear linear trend. In contrast, tensile residual stress increases the system's apparent fracture toughness in a more parabolic fashion: apparent fracture toughness initially increases with tensile residual stress but eventually peaks and declines beyond a certain point. The thicker film (Fig. 3b) exhibits a similar trend, albeit with a more significant slope. At the same tensile stress level, the thicker film can provide a higher toughening effect than the thin film. Furthermore, simulations with two levels of fracture energy for the film demonstrate that while compressive residual stress consistently reduced apparent toughness, higher fracture energy in the film leads to a greater increase in toughness under tensile stress.

It is important to note that the simulated tensile residual stress was capped at approximately 1000 MPa. This limitation was set because, in the simulations at higher tensile stress levels, cracks would likely initiate and propagate within the film itself during the thermal step. However, in the model, the cohesive element plane was positioned based on the assumption that cracks from indentation would propagate along the indenter edge, which does not accurately capture crack behavior driven by residual stress alone. Therefore, results related to high tensile stress were excluded, as they do not accurately represent realistic conditions.

3.1.2. Palmqvist crack geometry

When changing the property of the substrate material to develop Palmqvist crack, the Palmqvist cracks initiate near the free surface and propagate laterally within the coating (Movie S2). In our simulations, this behavior is captured by lateral crack growth confined to the film, with no interface decohesion, as perfect adhesion is assumed throughout. As a result, residual stress influences the cracking mechanism distinctly. To isolate the effect of the coating film's mechanical properties, the initial analysis considered a stress-free condition (Figure S2). The addition of a 50 nm film significantly reduces the splitting load by approximately 12%, whereas the 100 nm film has minimal impact on the critical load (Fig. 4). For thinner films, the substrate primarily dictates the mechanical response of the system due to its greater volume and structural dominance. Consequently, a low-toughness film provides minimal resistance to crack propagation, reducing the critical load required for crack initiation. However, as film thickness increases, the film's mechanical properties, particularly its strength and hardness, become more influential in resisting crack propagation. Thus, a thicker, stronger film enhances the system's overall fracture resistance, requiring a higher external load for crack initiation and propagation. The more detailed results are reported in the Supporting Information

Unlike median cracks, both compressive and tensile residual stresses in the film reduce the system's apparent resistance to crack propagation. Notably, while thinner stressed films exhibit a greater relative reduction in fracture toughness, they also display a shallower slope in this trend. This suggests that in the 50 nm film system, the primary reduction in fracture resistance arises from the film's lower mechanical toughness rather than the residual stress itself. In contrast, for thicker films, the residual stress plays a more significant role in influencing crack propagation resistance.

3.1.3. Fracture mechanism of the coated system

The simulation results indicate that surface residual stress state influences crack systems differently, as the driving force responsible for crack opening varies between systems. As illustrated in Fig. 5a, the median crack system typically forms beneath the plastic deformation zone under the indenter and propagates parallel to the loading axis. The primary driving force for crack propagation at the crack tip is the tensile stress surrounding the plastic deformation zone [39,40]. In terms of stress equilibrium across the whole system, tensile stress in the film induces a corresponding compressive stress within the substrate pillar. As a result, a higher external load is required to initiate and propagate the crack. Conversely, compressive stress within the film generates a tensile stress field in the substrate, which significantly weakens the system's resistance to crack propagation.

This apparent reduction in toughness with increasing compressive residual stress may seem counterintuitive when compared to classical multilayer systems, where compressive surface stress typically reduces crack driving forces. However, this effect arises from the specific geometry and constraint conditions of our system. In our case, the micropillar is coated conformally and constrained at its base, which imposes circumferential compatibility. As a result, compressive hoop stress in the ALD film induces a tensile stress field in the pillar core, enhancing the driving force for radial crack propagation. This mechanism differs fundamentally from planar multilayers under bending, as discussed in [14,15], where residual stress acts near the surface and shields the crack tip. In contrast, the high surface-to-volume ratio of our pillars leads to stress penetration into the full cross-section, and the observed trend is a direct consequence of the confined geometry.

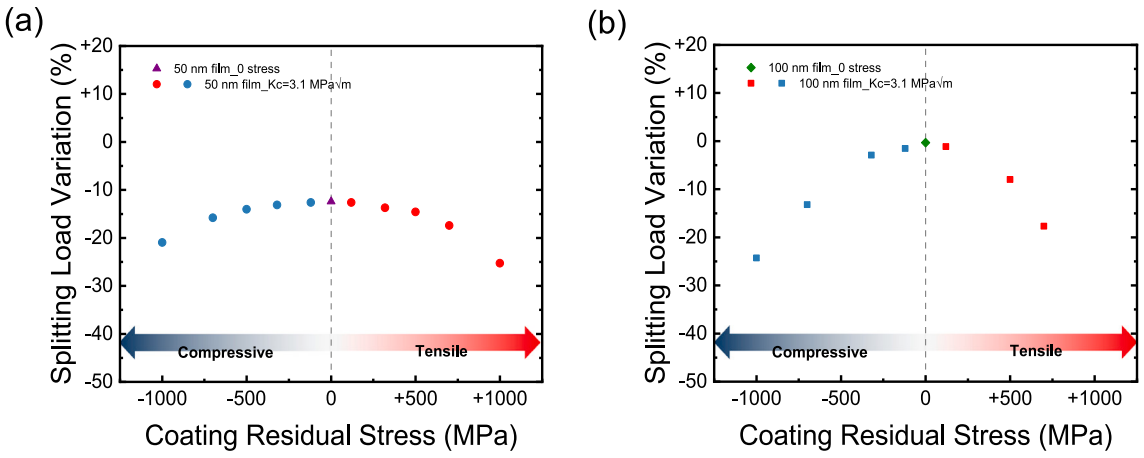

Fig. 4. The splitting load variation of the coated system with (a) 50 nm and (b) 100 nm ALD film on the ceramic substrate, which develops Palmqvist cracks as a function of the film residual stress.

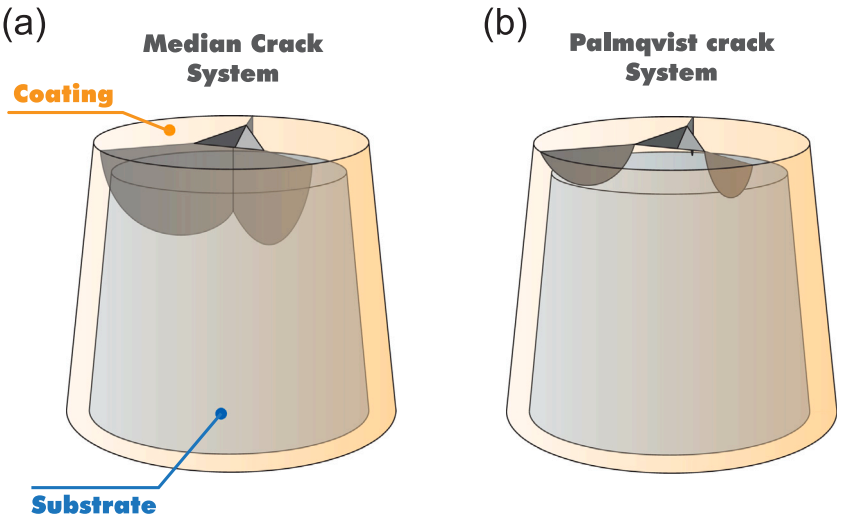

Fig. 5. Two cracking mechanisms achieved in ALD-coated pillars: (a) Median crack system develops through the substrate and reaches the coating; (b) Palmqvist crack system develops through the coating.

However, since the film cannot indefinitely sustain tensile residual stress, the toughening effect provided by residual stress is ultimately limited by the film's intrinsic fracture resistance (Figure S3, S4). When the residual stress approaches the failure threshold of the film, damage may accumulate during the thermal step, even if no visible cracking occurs. This pre-damaged state can trigger early crack initiation at the start of indentation, reducing the effectiveness of toughening. Additional simulations confirm that films with higher fracture toughness are better able to retain residual stress without early failure, allowing for greater stress transfer into the substrate. Details are provided in Supporting Information. Therefore, the extent of the toughening effect is not only governed by the magnitude of residual stress but also constrained by the crack resistance capability of the film itself.

In contrast to the median crack, the maximum tensile stress for the Palmqvist crack system is located near the surface rather than along the indentation axis, which makes the crack originate close to the surface and propagate laterally (Fig. 5b). When tensile residual stress is present in the film, it amplifies the tensile field near the surface, accelerating crack propagation and leading to complete fracture (Movie S3 and Figure S5). This effect reduces the critical load required for crack initiation, as the surface tensile stress makes the crack more likely to open and extend laterally (as shown in the Figure S5c-iv). Conversely, compressive residual stress in the film generates an opposing tensile stress within the substrate, which shifts the crack initiation zone from the surface to the subsurface region (Movie S4 and Figure S5c-iii). This shift indicates a transition from a Palmqvist to a median crack, driven by the inward tensile field. Consequently, compressive stress within the film detrimentally affects crack resistance by promoting subsurface crack development.

To isolate the geometric effect of the coating from the influence of residual stress, additional simulations were performed with coatings of varying thickness but zero residual stress (Supporting Information, Figure S1, S2). These results show that film thickness alone does not significantly alter the splitting load in the absence of residual stress. However, when residual stress is introduced (Figs. 3–4), the thicker films show a more pronounced reduction (in compressive cases) or increase (in tensile cases) in splitting load. This occurs because thicker coatings store more elastic energy and impose a stronger constraint or driving force onto the substrate, depending on the sign of the residual stress. The larger volume of stressed material in the thick coating amplifies the stress redistribution into the substrate, which in turn affects the crack driving force. This explains the observed trend of higher splitting-load sensitivity to residual stress in thicker films.

The simulation results show that the interaction between residual stress and crack propagation mechanisms is highly dependent on crack geometry, stress distribution, and film thickness. Stress equilibrium across the substrate-film system influences median cracks, while the

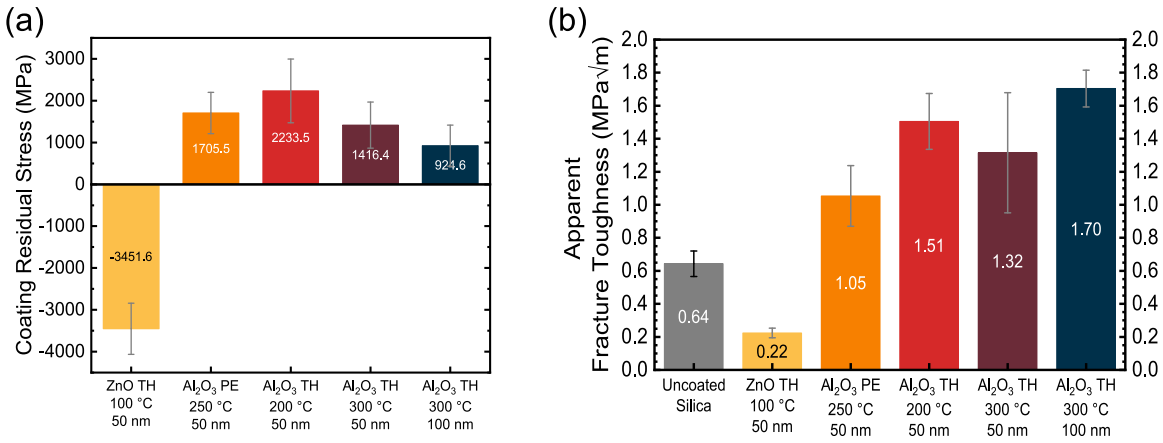

Fig. 6. (a) The residual stress of the ALD coating on fused silica substrates; and (b) the apparent fracture toughness of ALD-coated fused silica as a function of the deposition parameters. Error bars represent the standard deviation from multiple measurements, and are presented in the same manner for the figures below.

surface stress fields influence Palmqvist cracks. These findings highlight the complex role of thin film residual stress in governing crack initiation and propagation, emphasizing the importance of tailoring stress levels and film properties to enhance system resistance against fracture. This is of predominant prevalence in the case of coated micro-architectures.

3.2. Experimental validation

3.2.1. Fused silica

The residual stresses of ultra-thin ALD films on the two substrates were measured as a function of deposition parameters using the FIB-DIC method. Details of the stress calculation process are provided in Supporting information. Among the samples, only the 50 nm ZnO film on the fused silica substrate exhibited compressive residual stress, measured at -3100 ± 610 MPa (Fig. 6a). In contrast, all Al_2O_3 films on fused silica exhibited tensile residual stress (Fig. 6a). The highest residual stress, 2233 ± 763 MPa, was observed for the 50 nm Al_2O_3 film grown at 200 °C on the fused silica substrate. The thicker Al_2O_3 films grown at 300 °C showed slightly lower residual stress values than the 50 nm Al_2O_3 film.

As shown in Figure S9, the loading curves of different tests for each sample show consistent tendencies, indicating that the position error coming from ex-situ tests was in the acceptable range for the pillar splitting method [37]. The scatter of critical instability load mainly depends on the individual differences between tested pillars. A slight pop-in plateau was observed for uncoated fused silica samples before the complete failure, which only happened on the ZnO-coated fused silica and Al_2O_3 grown using the plasma-enhanced technique. The pop-in event in ZnO-coated fused silica occurred even earlier than in the uncoated fused silica.

In this study, we considered the uncoated substrate to be the primary contributor to the mechanical response of the coated system, due to its significantly larger volume compared to the 50 nm thick ALD film. As a result, we applied the same γ coefficient, 0.56 for fused silica to both the uncoated and coated samples. This γ value was determined from the modulus and hardness of the uncoated substrate using CSM measurements. While the presence of a thin coating may slightly influence the near-surface mechanical response, its impact on the overall E/H ratio is minimal in this configuration. Even when Palmqvist cracks initiate partially within the coating, the path of the crack and the energy dissipation are largely dictated by the substrate. This assumption is supported by Xia et al. [41], who demonstrated that the composite E/H ratio remains effectively unchanged for coated systems when the thickness of the coating is small relative to the indentation depth and the dimensions of the substrate. Since we are focused on the apparent fracture toughness of the coated system, rather than the intrinsic properties of the film, we maintained a constant γ value to ensure consistency across different coating conditions. The apparent fracture toughness was calculated from Eq. (3). All the samples with ALD coatings exhibited higher apparent fracture toughness compared to the uncoated fused silica (Fig. 6b), except the 50 nm ZnO film resulted in a reduction. The samples with a 100 nm Al_2O_3 film grown at 300 °C demonstrated nearly three times the apparent fracture toughness of the uncoated fused silica. The 50 nm Al_2O_3 film, grown at the same temperature, showed lower apparent fracture toughness than the thicker coating but exhibited the biggest scatter in the critical load values. For a pillar coated with a 50 nm Al_2O_3 film at 300 °C, a splitting test was intentionally halted before fracture by setting the maximum load lower than the critical load. Indentation marks and focused ion beam (FIB) cross-section analysis of the residual indentation imprints revealed the presence of median cracks in the fused silica substrate (Movie S5, Fig. 7a). These cracks were observed in the cross-sectional view perpendicular to the indenter edge, where the crack openings extend beneath the contact surface with the indenter.

3.2.2. Glassy carbon

Fig. 8a illustrates the residual stress profiles for different coating parameters on the GC substrate. A similar trend was observed with the fused silica substrate: the 50 nm Al_2O_3 film grown at 200 °C exhibited the highest tensile residual stress. However, the stress reached only around 870 MPa, approximately one-third of the value observed on the fused silica substrate under identical deposition conditions. The other Al_2O_3 films also exhibited lower residual stress when deposited on the glassy carbon substrate compared to those on fused silica. Furthermore, Al_2O_3 films fabricated using plasma-enhanced ALD showed lower tensile stress compared to their thermally deposited counterparts at the same deposition temperature.

In contrast to the performance of ALD-coated fused silica, the pop-in plateau was observed in most of the ALD-coated samples but not the pristine glassy carbon pillars (Figure S10), indicating the early crack during the pillar splitting tests after adding the ultra-thin Al_2O_3 film. As clarified in Section 3.2.1, here the gamma coefficient of 0.19 was used to calculate the apparent fracture toughness of the uncoated and coated glassy carbon samples [13]. Each type of coating film led to a reduction of K_c value compared with the uncoated status (Fig. 8b). The 50 nm Al_2O_3 film grown at 200 °C caused the most significant loss. The other two Al_2O_3 films, deposited by plasma-enhanced ALD at 200 °C and thermal ALD at 350 °C, resulted in slight reductions in fracture toughness. Fig. 7b shows not only median cracks, but also cone cracks in the contact surface of the GC micro-pillar coated with Al_2O_3 film, which is consistent with the crack geometry of uncoated GC [13].

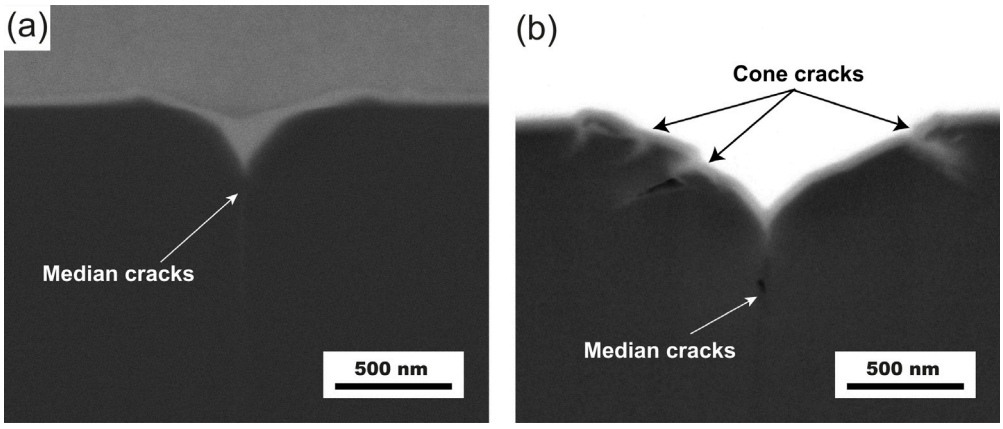

Fig. 7. FIB cross-section of the indent just before splitting failure of the (a) fused silica coated with 50 nm Al_2O_3 at 300 °C; (b) glassy carbon coated with 50 nm Al_2O_3 via PE-ALD.

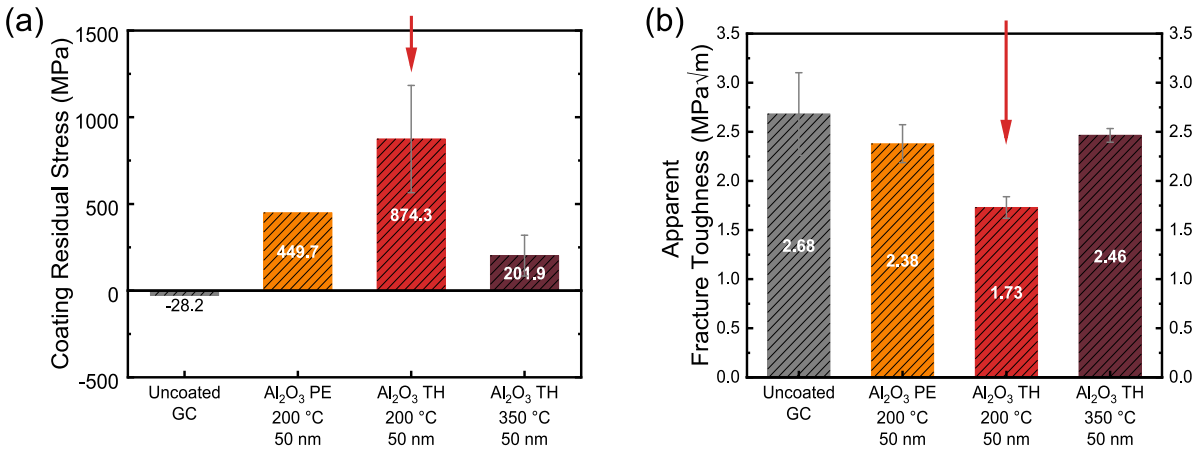

Fig. 8. (a) The residual stress of the ALD coating on glassy carbon substrates; and (b) the apparent fracture toughness of ALD coated glassy carbon as a function of the deposition parameters. (The red arrow was used to highlight the sample showing highest stress level and lowest apparent fracture toughness).

Fig. 9 illustrates the relationship between apparent fracture toughness and residual stress, with the right axis indicating the relative change in apparent fracture toughness compared to the uncoated sample. For the 50 nm Al_2O_3 film on a fused silica substrate, the apparent fracture toughness increases with tensile residual stress. The Al_2O_3 film deposited at 200 °C exhibited the highest tensile residual stress, leading to an approximate 140% improvement in system fracture toughness. Interestingly, the 100 nm Al_2O_3 film deposited at 300 °C showed the lowest tensile residual stress than other films but provided the highest toughening effect, demonstrating a substantial 165% increase in fracture toughness compared to uncoated fused silica. In contrast, ZnO films, which exhibited compressive stress, displayed a different behavior. "Pop-in" events were observed around 300 nm in the load–displacement curves, indicating the initiation of early cracks during pillar splitting tests. From Fig. 9b, all the tensile stresses in Al_2O_3 film resulted in a reduction in the fracture toughness of ALD-coated GC compared with the uncoated one, showing a reverse tendency for the fused silica. Although the apparent fracture toughness values for the PE 200 °C and TH 350 °C Al_2O_3-coated samples show only modest reductions compared to the uncoated glassy carbon and fall within the bounds of experimental scatter, they remain fully consistent with the monotonic trend observed in both the normalized toughness plot (Fig. 9b) and the FEM simulations. The PE 200 °C and TH 350 °C coatings induce moderate tensile residual stresses that, while lower in magnitude, still contribute to an increase in the crack driving force. In glassy carbon, which exhibits flaw-sensitive fracture, the influence of residual stress on toughness becomes increasingly apparent only when the stress field reaches a scale comparable to the crack tip energy release rate. This explains why the largest reduction is observed in the TH 200 °C sample, which exhibits the highest tensile stress (874 MPa). The overall behavior confirms that the effect of residual stress on fracture is progressive and mechanically driven, even if not all intermediate steps are statistically resolved in isolation.

4. Discussion

4.1. Residual stress from ALD coating process

Importantly, ALD-deposited Al_2O_3 films are more accurately represented as amorphous AlO_xH_y, especially when deposited at lower temperatures (e.g., ~200 °C). These films are hydroxyl-rich and exhibit incomplete network formation due to low atomic mobility during deposition, leading to limited structural relaxation. This chemical and structural nature plays a central role in the development of intrinsic tensile stresses [42]. Residual stress in ALD coatings originates primarily from two mechanisms: growth-induced stress and thermal stress. Growth-induced stress is dominant and stems from ALD's self-limiting, layer-by-layer deposition process, where each cycle incrementally introduces strain that accumulates with increasing film thickness. This stress is exacerbated in thinner films due to fewer opportunities for relaxation. Strategies such as plasma-enhanced ALD, thermal ALD at high temperature, and increased film thickness can improve network condensation, reduce hydroxyl content, enhance film densification, and facilitate stress relaxation—all of which contribute to reducing

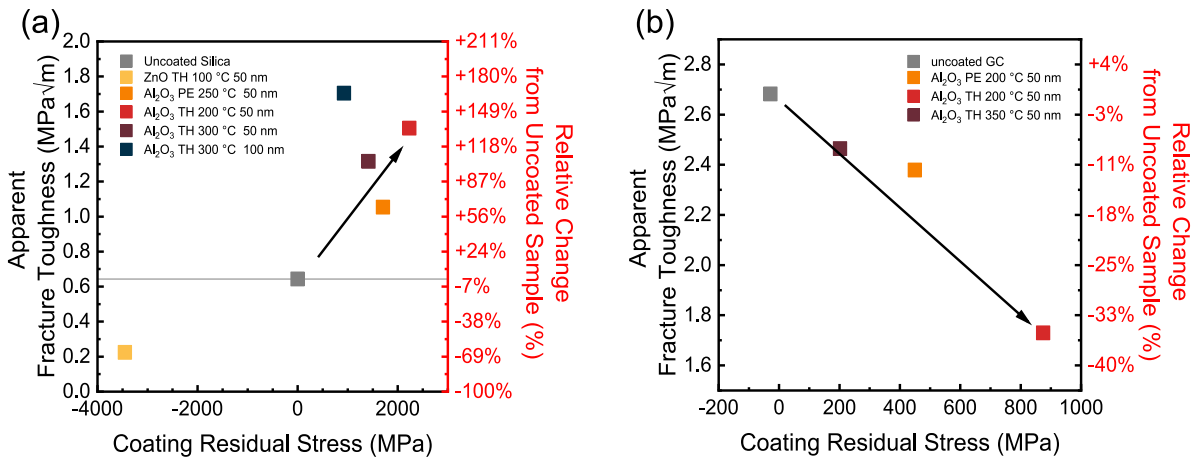

Fig. 9. The apparent fracture toughness as a function of the residual stress of ALD film on (a) fused silica and (b) GC substrate. Error bars are omitted for clarity, as they have been presented in Fig. 6 and Fig. 8 above.

growth-induced stress, as corroborated by our FIB-DIC results. In comparison, thermal stress arises from mismatches in the thermal expansion coefficients between the film and the substrate during cooling from deposition temperatures. This can be estimated through Equation (1). Using representative thermal expansion values, fused silica ($\alpha_{s1} \approx 0.5 \times 10^{-6}K^{-1}$) [43], glassy carbon ($\alpha_{s2} \approx 4.3 \times 10^{-6}K^{-1}$) [44], and ALD-grown Al_2O_3 ($\alpha_f \approx 4.2 \times 10^{-6}K^{-1}$) [42], and considering deposition temperatures between 200 °C to 300 °C, the resulting thermal stress is estimated at ~130 MPa to 250 MPa on fused silica and near-zero on glassy carbon. Since this accounts for only 10%–20% of the total tensile stress observed, it confirms that growth-induced stress is the dominant component in our films. It is important to note that the residual stresses measured in each film are not microstructurally independent quantities. On the contrary, they arise from the intrinsic evolution of density, porosity, hydrogen incorporation, and interfacial bonding during ALD growth, as discussed in prior studies [42,45]. In this sense, residual stress functions as a microstructurally-integrated parameter that captures the net mechanical effect of these nanoscale features. Cross-sectional TEM confirmed that all coatings were fully amorphous and well adhered to the substrate (Figure S6), supporting the use of residual stress as a robust, quantitative descriptor linking film structure to fracture behavior.

The experimental results align with these mechanisms. The plasma in PE-ALD of Al_2O_3 promotes more complete surface reactions and enhances film densification of Al_2O_3, leading to reduced residual stress levels compared with those in thermally grown films [46]. Films deposited at 300 °C exhibited the lowest residual stress, attributed to improved growth uniformity and enhanced stress relaxation enabled by the elevated deposition temperature. Conversely, the 50 nm Al_2O_3 film deposited at 200 °C displayed the highest residual stress, reaching nearly 2233 MPa. This elevated stress level likely arises from incomplete film densification and greater strain accumulation due to the lower deposition temperature, which limits stress relaxation. The measured residual stress values in this study significantly exceed those reported in previous works [42,46–48], a discrepancy that can be attributed to the unique properties of ultra-thin films. Ultra-thin Al_2O_3 films deposited via ALD are well-known for their exceptional mechanical performance, which allows them to sustain extraordinarily high residual stresses without failure. For instance, these films can endure residual stresses of up to 6 GPa [49] and demonstrate strengths of approximately 5.5 GPa in bulge tests [50], values that are nearly 20 times higher than those of bulk Al_2O_3. This remarkable resilience is primarily due to the unique mechanical characteristics of ultra-thin films. Unlike bulk materials, these films exhibit elevated elastic limits and improved resistance to crack propagation arising from their nanoscale dimensions and geometrical constraints. While ALD's layer-by-layer growth offers excellent control over film thickness and uniformity, the resulting structure is not necessarily densely packed. Elastic strain and the presence of hydroxyl groups can lead to slight structural openness or nanoporosity. Nevertheless, the high uniformity and low defect density achieved in ALD films contribute to their impressive mechanical robustness, enabling them to sustain stress levels far exceeding those of bulk Al_2O_3. These findings emphasize the critical interplay between thickness, deposition temperature, and growth mechanisms in determining the stress behavior of ALD-grown films.

Since glassy carbon has a lower elastic modulus compared to fused silica, the GC substrate can undergo more significant elastic deformation under stress. This enhanced deformability allows GC to accommodate better and dissipate stresses that develop during film deposition and subsequent thermal cycling, reducing the buildup of residual stress within the film. Additionally, the thermal expansion coefficient mismatch between GC and Al_2O_3 is smaller than that between fused silica and Al_2O_3. As a result, Al_2O_3 films on GC substrates exhibit the same trend in residual stress behavior but with consistently lower values compared to films on fused silica substrates.

At low temperatures, ZnO tends to grow in an amorphous state, especially when the film thickness is thin, as thinner layers inhibit crystallinity [51]. In this study, an ultra-thin amorphous ZnO film was created under the low-temperature deposition (100 °C). Unlike Al_2O_3 films, ZnO has a relatively higher atomic packing density compared to many substrates, which induces compressive residual stress. This compressive stress becomes more pronounced as film thickness decreases due to limited relaxation pathways in thinner films [52].

4.2. Fracture mechanism of ALD coated glassy-carbon and fused silica

Fig. 9 illustrates the distinct effects of residual stress on the fracture mechanisms of fused silica and glassy carbon, which is related to their different crack geometry in Fig. 7. The observed trends align well with FEM simulation results, where the median-mode cracking in fused silica was influenced by stress distribution. Tensile stress in the Al_2O_3 film contributes to compressive stress in the substrate, leading to a toughening effect for the entire system in the case of median crack geometry. Conversely, compressive stress in the film induces tensile stress in the substrate, which can trigger early cracks, as seen in the ZnO-coated samples during pillar splitting tests. Notably, the 100 nm -thick Al_2O_3 coating deposited at 300 °C exhibits a significantly higher apparent fracture toughness compared to the 50 nm coating at

similar residual stress levels. While FEM simulations predict a modest increase in splitting load (less than 5%) due to geometric effects alone, the experimentally observed enhancement is substantially larger. This suggests that additional energy dissipation mechanisms may be active in thicker coatings. Possible contributors include localized plasticity, partial interface sliding, or distributed microcracking within the amorphous Al_2O_3 film. Such effects can redistribute stress near the crack tip, thereby delaying the onset of fracture. Although not explicitly modeled in the present framework, these mechanisms are plausible under high constraint and tensile stress in thicker films and likely contribute to the enhanced crack resistance observed experimentally.

However, the experimentally observed gains in fracture toughness for samples under tensile stress were significantly higher than those predicted by FEM simulations. This discrepancy arises because the simulation employs restricted constraint conditions, such as simplified fracture energy and critical plane assumptions, to streamline the analysis. These simplifications, while necessary for computational feasibility, can introduce artificial artifacts that deviate from real-world behavior. For instance, ultrathin Al_2O_3 films may exhibit enhanced crack resistance at the nanoscale [49,50], allowing them to sustain higher tensile stress and, in turn, enabling greater compressive stress to be transferred into the pillar, thereby further toughening the system, while this is limited in the simulation (Figure S3-4). Furthermore, additional complexities such as interfacial sliding, distributed microcracking, or time-dependent stress relaxation were not implemented in the current model to maintain a well-controlled and interpretable simulation framework, which would make the simulation underestimate the toughening effect in real situation

In the simulation, the toughening effect begins to diminish at higher tensile stress levels (Fig. 3), primarily due to the film approaching its fracture limit and accumulating pre-damage, this trend was not evident in the experimental data within the tested stress range. One possible explanation is that the fracture toughness of the actual ALD film may exceed the conservative values used in the simulation, allowing it to withstand greater tensile stress without initiating early failure. As a result, the toughening effect in experiments continued to increase, whereas the simulation predicted an eventual plateau or decline.

Another noteworthy point is the noticeable variation observed in the sample with a 50 nm film deposited at 300 °C highlighting the system's sensitivity to processing conditions and local stress states. This sample lies in a transitional regime, combining moderate tensile residual stress (around 1150 MPa) with intermediate film toughness. Although neither parameter is extreme, their interplay creates a stress-sensitive condition where small variations in thickness, interfacial quality, or film properties can significantly alter crack initiation and stress redistribution. This underscores the need for further studies on the size- and processing-dependent fracture behavior of ultrathin films and the development of models capable of capturing spontaneous cracking and complex failure processes.

Different from the fused silica, the cone crack system in the near-surface of the coated GC micro-pillars makes the residual stress play a different role in the mechanism. In the cone crack system, ring cracks initiate due to high tensile stress near the contact edge, which can be observed on the contact surface. Given the similarities between cone cracks and Palmqvist cracks, that both of them initiate near the free surface and are driven by tensile hoop stress, the GC is expected to behave similarly to a substrate that develops Palmqvist cracks under residual stress. So, the tensile stress in the film would result in the early cracks and speed up the fracture behavior, leading to embrittlement.

It is also worth noting that while localized densification of the amorphous AlO_xH_y coating under indentation is theoretically possible—particularly under the high stress concentration of a cube-corner indenter, its effect is expected to be limited in fused silica samples. In these cases, fracture occurs predominantly within the substrate (via median cracking), and the coating primarily modulates the residual stress environment. However, for glassy carbon substrates, where surface-initiated cracks (e.g., Palmqvist or cone-like) dominate, the stress field from indentation may interact more significantly with the coating. Local densification of the amorphous layer could reduce compressive constraint in the vicinity of the indentation site, thereby contributing to the observed reduction in apparent toughness enhancement in coated GC samples.

4.3. Generalization to complex shaped coated architectures

In this study, core–shell pillars were selected as a simplified 3D model to analyze the effects of residual stress through a pillar splitting test, which offers a well-controlled experimental approach to understanding the fracture mechanism. The test results indicate that multiple factors, including substrate mechanical properties, crack geometry, film thickness, and surface residual stress govern crack propagation resistance. In particular, crack geometry plays a critical role in determining how residual stress affects crack propagation, as different crack shapes and orientations can lead to varying fracture behaviors.

While simple pillar structures provide fundamental insights, real-world applications demand the use of more complex micro-architectures, often realized through advanced fabrication techniques such as 3D printing. In these architected materials, residual stress interacts with geometric features to create unique mechanical responses. Unlike homogeneous materials, micro-lattices feature nodes and trusses with varying stress concentrations. Stress concentrations influence the mechanical behavior of nanolattice architectures and crack initiation sites, which predominantly occur at structural junctions. For example, In rigid stretching-dominated architectures, such as octet-truss lattices, nodes experience higher stress concentrations due to force transmission across multiple trusses, making them the most vulnerable points for crack initiation. Optimizing stress distribution at these locations is crucial for improving the mechanical resilience of the structure. This work provides another potential approach regarding interface engineering, aside from topology design, to improve mechanical reliability.

Building upon the results from the pillar splitting test, it is evident that different residual stress states can significantly affect crack resistance. By controlling the residual stress distribution within micro-architectured metamaterials, it is possible to enhance mechanical properties strategically. For instance, introducing beneficial compressive stress at the weakest points through surface tensile residual stress, such as nodes in rigid stretching-dominated structures, can enhance their toughness. Simultaneously, leaving less advantageous stress states in non-critical regions minimizes potential failure risks without compromising the overall performance of the material.

Future advancements should focus on integrating computational modeling and experimental approaches to engineer residual stress distributions in these complex architectures precisely. By leveraging advanced fabrication techniques, such as controlled thermal treatments and stress-engineered deposition processes, tailored stress states can be achieved. This approach holds significant promise for designing high-performance, damage-tolerant metamaterials suitable for structural, aerospace, and biomedical applications.

5. Conclusions

This study investigated the influence of ALD coatings on the crack propagation resistance of core–shell 3D-printed fused silica and glassy carbon micro-ceramics, with a specific focus on Al_2O_3 and ZnO coatings produced via thermal and plasma-enhanced ALD. High-resolution FIB-DIC measurements provided critical data on residual stress evaluation. By utilizing the pillar splitting method, it was observed that ALD coatings can either enhance or degrade apparent fracture toughness depending on the material and stress level. CZ-FEM models were used to incorporate with the experiment and help understand fracture mechanisms deeper.

Firstly, FEM simulations highlight the dual effects of ALD-induced residual stress on crack behavior. Tensile stress in the coating is shown to enhance the apparent fracture toughness of the system when median cracks are present since it induces compressive stress in the underlying material, whereas compressive stress causes a reduction. Conversely, both tensile and compressive residual stresses lead to embrittlement when Palmqvist cracks develop in the substrate.

Experimental synthesis demonstrates that fused silica micro-pillars achieved remarkable toughness gains of 134% with 50 nm Al_2O_3 coatings at 200 °C, driven by the large tensile residual stress in the film. In contrast, 100 nm Al_2O_3 coatings at 300 °C led to a 165% increase in toughness, attributed to the thicker film compensating for the smaller residual stress. On the contrary, the ZnO coating film with compressive stress induced the early crack of fused silica micropillars. However, glassy carbon micro-pillars exhibited a reduction in apparent fracture toughness due to the tensile stress of Al_2O_3 coating and its cone crack geometry. This underscores the material-specific responses to ALD coatings and residual stress effects.

By integrating experimental and computational approaches, this work advances the understanding of residual stress and its role in the fracture behavior of micro-ceramic systems. This observation highlights the tremendous potential of stress engineering via ALD coatings to fine-tune the fracture toughness and improve mechanical reliability. The next step would be to promote these strategies to micro-architected metamaterials and take into account both the interface engineering and the topology structures.

Supplementary materials

Supplementary material associated with this article can be found, in the online version

CRediT authorship contribution statement

Wenjuan Cheng: Writing – review & editing, Writing – original draft, Visualization, Validation, Methodology, Investigation, Data curation. **Edoardo Rossi:** Writing – review & editing, Writing – original draft, Visualization, Validation, Methodology, Investigation, Formal analysis, Data curation, Conceptualization. **Jens Bauer:** Writing – review & editing, Supervision, Resources, Methodology, Funding acquisition, Conceptualization. **Jose Paolo Martins:** Writing – review & editing, Resources, Methodology. **Raphael Guillemet:** Writing – review & editing, Resources, Methodology. **Laszlo Pethö:** Writing – review & editing, Validation, Resources, Methodology. **Johann Michler:** Writing – review & editing, Validation, Supervision, Resources. **Marco Sebastiani:** Writing – review & editing, Writing – original draft, Validation, Supervision, Methodology, Funding acquisition, Conceptualization.

Declaration of competing interest

The authors declare that they have no known competing financial interests or personal relationships that could have appeared to influence the work reported in this paper.

Acknowledgments

W. Cheng, E. Rossi, and M. Sebastiani gratefully acknowledge financial support from the national project, titled "Strong Nano-Architected Materials by ResIdual StrEss control (SuNRISE)" (Grant Agreement No. FIS-2023-03472), funded by the Italian Ministry of University and Research (MUR). J. Bauer acknowledges support from the German Research Foundation (DFG) grant BA 5778/2-1.

Appendix A. Supplementary data

Supplementary material related to this article can be found online at https://doi.org/10.1016/j.actamat.2025.121474.

References

[1] J. Bauer, L.R. Meza, T.A. Schaedler, R. Schwaiger, X. Zheng, L. Valdevit, Nanolattices: An emerging class of mechanical metamaterials, 2017/09/06, Adv. Mater. 29 (2017) 1–26.
[2] J. Bauer, A. Schroer, R. Schwaiger, O. Kraft, Approaching theoretical strength in glassy carbon nanolattices, 2016/02/02, Nat. Mater. 15 (2016) 438–443.
[3] C. Crook, J. Bauer, A.G. Izard, C.S. de Oliveira, J.M. de Souza e Silva, J.B. Berger, L. Valdevit, Plate-nanolattices at the theoretical limit of stiffness and strength, Nat. Commun. 11 (2020).
[4] X. Chen, J. Moughames, Q. Ji, J.A.I. Martínez, H. Tan, G. Ulliac, V. Laude, M. Kadic, 3D lightweight mechanical metamaterial with nearly isotropic inelastic large deformation response, J. Mech. Phys. Solids 169 (2022).
[5] L. Wang, G. Ulliac, B. Wang, J.A.I. Martínez, K.K. Dudek, V. Laude, M. Kadic, 3D auxetic metamaterials with elastically-stable continuous phase transition, Adv. Sci. 9 (2022).
[6] J. Bauer, J.A. Kraus, C. Crook, J.J. Rimoli, L. Valdevit, Tensegrity metamaterials: Toward failure-resistant engineering systems through delocalized deformation, Adv. Mater. 33 (2021).
[7] W.P. Moestopo, A.J. Mateos, R.M. Fuller, J.R. Greer, C.M. Portela, Pushing and pulling on ropes: Hierarchical woven materials, Adv. Sci. 7 (2020).
[8] T. Juarez, A. Schroer, R. Schwaiger, A.M. Hodge, Evaluating sputter deposited metal coatings on 3D printed polymer micro-truss structures, Mater. Des. 140 (2018) 442–450.
[9] J.U. Surjadi, X. Feng, W. Zhou, Y. Lu, Optimizing film thickness to delay strut fracture in high-entropy alloy composite microlattices, Int. J. Extrem. Manuf. 3 (2021).
[10] X. Feng, J.U. Surjadi, R. Fan, X. Li, W. Zhou, S. Zhao, Y. Lu, Microalloyed medium-entropy alloy (MEA) composite nanolattices with ultrahigh toughness and cyclability, Mater. Today 42 (2021) 10–16.
[11] R.W. Johnson, A. Hultqvist, S.F. Bent, A brief review of atomic layer deposition: from fundamentals to applications, Mater. Today 17 (5) (2014) 236–246.
[12] J. Bauer, A. Schroer, R. Schwaiger, O. Kraft, The impact of size and loading direction on the strength of architected lattice materials, Adv. Eng. Mater. 18 (2016) 1537–1543.
[13] E. Rossi, J. Bauer, M. Sebastiani, Humidity-dependent flaw sensitivity in the crack propagation resistance of 3D-printed nano-ceramics, Scr. Mater. 194 (2021).
[14] M. Lugovy, V. Slyunyayev, N. Orlovskaya, G. Blugan, J. Kuebler, M. Lewis, Apparent fracture toughness of si3n4-based laminates with residual compressive or tensile stresses in surface layers, Acta Mater. 53 (2) (2005) 289–296.
[15] Z. Xia, W. Curtin, B. Sheldon, A new method to evaluate the fracture toughness of thin films, Acta Mater. 52 (12) (2004) 3507–3517, URL https://www.sciencedirect.com/science/article/pii/S1359645404002083.
[16] A.J.D. Shaikeea, H. Cui, M. O'Masta, X.R. Zheng, V.S. Deshpande, The toughness of mechanical metamaterials, Nat. Mater. 21 (3) (2022) 297–304.
[17] A.J. Mateos, W. Huang, Y.-W. Zhang, J.R. Greer, Discrete-continuum duality of architected materials: Failure, flaws, and fracture, Adv. Funct. Mater. 29 (5) (2019) 1806772.
[18] S.M. Sajadi, L. Vásárhelyi, R. Mousavi, A.H. Rahmati, Z. Kónya, Á. Kukovecz, T. Arif, T. Filleter, R. Vajtai, P. Boul, Z. Pang, T. Li, C.S. Tiwary, M.M. Rahman, P.M. Ajayan, Damage-tolerant 3D-printed ceramics via conformal coating, Sci. Adv. 7 (28) (2021) eabc5028.
[19] A.M. Korsunsky, M. Sebastiani, E. Bemporad, Focused ion beam ring drilling for residual stress evaluation, Mater. Lett. 63 (22) (2009) 1961–1963.
[20] M. Sebastiani, C. Eberl, E. Bemporad, G.M. Pharr, Depth-resolved residual stress analysis of thin coatings by a new FIB–DIC method, Mater. Sci. Eng.: A 528 (27) (2011) 7901–7908.
[21] A. Korsunsky, E. Salvati, A. Lunt, T. Sui, M. Mughal, R. Daniel, J. Keckes, E. Bemporad, M. Sebastiani, Nanoscale residual stress depth profiling by focused ion beam milling and eigenstrain analysis, Mater. Des. 145 (2018) 55–64.
[22] E. Salvati, L. Romano-Brandt, M. Mughal, M. Sebastiani, A. Korsunsky, Generalised residual stress depth profiling at the nanoscale using focused ion beam milling, J. Mech. Phys. Solids 125 (2019) 488–501.
[23] M. Sebastiani, K.E. Johanns, E.G. Herbert, F. Carassiti, G.M. Pharr, A novel pillar indentation splitting test for measuring fracture toughness of thin ceramic coatings, Phil. Mag. 95 (2015) 1928–1944.
[24] Abaqus finite element analysis | SIMULIA - dassault systèmes, 2024, https://www.3ds.com/products/simulia/abaqus. (Accessed: 17 October 2024).
[25] K.E. Johanns, J.H. Lee, Y.F. Gao, G.M. Pharr, An evaluation of the advantages and limitations in simulating indentation cracking with cohesive zone finite elements, Modelling Simul. Mater. Sci. Eng. 22 (2014).
[26] S. Bruns, K.E. Johanns, H.U. Rehman, G.M. Pharr, K. Durst, Constitutive modeling of indentation cracking in fused silica, J. Am. Ceram. Soc. 100 (2017) 1928–1940.
[27] J.O. Carneiro, V. Teixeira, S. Azevedo, Residual stresses in thin films evaluated by different experimental techniques, in: R.B. Hetnarski (Ed.), Encyclopedia of Thermal Stresses, Springer Netherlands, Dordrecht, 2014, pp. 4222–4231.
[28] J. Ast, M. Ghidelli, K. Durst, M. Göken, M. Sebastiani, A. Korsunsky, A review of experimental approaches to fracture toughness evaluation at the micro-scale, Mater. Des. 173 (2019) 107762.

[29] M. Ghidelli, M. Sebastiani, K.E.K. Johanns, G.M.G. Pharr, Effects of indenter angle on micro-scale fracture toughness measurement by pillar splitting, J. Am. Ceram. Soc. 100 (2017) 5731–5738.
[30] T. Beirau, E. Rossi, M. Sebastiani, W.C. Oliver, H. Pöllmann, R.C. Ewing, Fracture toughness of radiation-damaged zircon studied by nanoindentation pillar-splitting, Appl. Phys. Lett. 119 (23) (2021) 231903.
[31] S. Bruns, L. Petho, C. Minnert, J. Michler, K. Durst, Fracture toughness determination of fused silica by cube corner indentation cracking and pillar splitting, Mater. Des. 186 (2020).
[32] W. Oliver, G. Pharr, An improved technique for determining hardness and elastic modulus using load and displacement sensing indentation experiments, J. Mater. Res. 7 (1992) 1564–1583.
[33] M.F. Doerner, W.D. Nix, A method for interpreting the data from depth-sensing indentation instruments, J. Mater. Res. 1 (1986) 601–609.
[34] A. Korsunsky, M. McGurk, S. Bull, T. Page, On the hardness of coated systems, Surf. Coat. Technol. 99 (1) (1998) 171–183.
[35] J. Bauer, A. Schroer, R. Schwaiger, O. Kraft, The impact of size and loading direction on the strength of architected lattice materials, Adv. Eng. Mater. 18 (9) (2016) 1537–1543.
[36] J. Zhao, R. Bradt, P. Walker, The fracture toughness of glassy carbons at elevated temperatures, Carbon 23 (1) (1985) 15–18.
[37] C.M. Lauener, L. Petho, M. Chen, Y. Xiao, J. Michler, J.M. Wheeler, Fracture of silicon: Influence of rate, positioning accuracy, FIB machining, and elevated temperatures on toughness measured by pillar indentation splitting, Mater. Des. 142 (2018) 340–349.
[38] B. Winiarski, G.S. Schajer, P.J. Withers, Surface decoration for improving the accuracy of displacement measurements by digital image correlationin SEM, in: T. Proulx (Ed.), in: Application of Imaging Techniques To Mechanics of Materials and Structures, vol. 4, Springer New York, New York, NY, 2013, pp. 217–224.
[39] J. Chen, Indentation-based methods to assess fracture toughness for thin coatings, J. Phys. D: Appl. Phys. 45 (20) (2012) 203001.
[40] G. Okuma, K. Maeda, S. Yoshida, A. Takeuchi, F. Wakai, Morphology of subsurface cracks in glass-ceramics induced by vickers indentation observed by synchrotron X-ray multiscale tomography, Sci. Rep. 12 (2022).
[41] Y. Xia, L. Zhang, L. Hu, Y. Liu, L. He, J. Tan, Z. Wang, Investigation of fracture toughness and microstructure of micro-scaled multilayer-DLC/silicon system via pillar splitting method, Ceram. Int. 49 (23, Part B) (2023) 38662–38671.
[42] O.M. Ylivaara, X. Liu, L. Kilpi, J. Lyytinen, D. Schneider, M. Laitinen, J. Julin, S. Ali, S. Sintonen, M. Berdova, E. Haimi, T. Sajavaara, H. Ronkainen, H. Lipsanen, J. Koskinen, S.P. Hannula, R.L. Puurunen, Aluminum oxide from trimethylaluminum and water by atomic layer deposition: The temperature dependence of residual stress, elastic modulus, hardness and adhesion, Thin Solid Films 552 (2014) 124–135.
[43] J. Oishi, T. Kimura, Thermal expansion of fused quartz, Metrologia 5 (2) (1969) 50.
[44] D.D. Markushev, J. Ordonez-Miranda, M.D. Rabasović, M. Prelas, J.F. O'Hara, J.A. Woollam, J.A. Pérez-Hernández, B. Pal, M.S. Jovanović, M.M. Gvozdenović, Thermal and elastic characterization of glassy carbon thin films by photoacoustic measurements, Eur. Phys. J. Plus 132 (2) (2017) 33.
[45] O.M. Ylivaara, A. Langner, X. Liu, D. Schneider, J. Julin, K. Arstila, S. Sintonen, S. Ali, H. Lipsanen, T. Sajavaara, S.-P. Hannula, R.L. Puurunen, Mechanical and optical properties of as-grown and thermally annealed titanium dioxide from titanium tetrachloride and water by atomic layer deposition, Thin Solid Films 732 (2021) 138758.
[46] S. Shestaeva, A. Bingel, P. Munzert, L. Ghazaryan, C. Patzig, A. Tünnermann, A. Szeghalmi, Mechanical, structural, and optical properties of PEALD metallic oxides for optical applications, Appl. Opt. 56 (2017) C47.
[47] O.M.E. Ylivaara, L. Kilpi, X. Liu, S. Sintonen, S. Ali, M. Laitinen, J. Julin, E. Haimi, T. Sajavaara, H. Lipsanen, S.-P. Hannula, H. Ronkainen, R.L. Puurunen, Aluminum oxide/titanium dioxide nanolaminates grown by atomic layer deposition: Growth and mechanical properties, J. Vac. Sci. Technol. A: Vac. Surfaces, Films 35 (2017).
[48] D.C. Miller, R.R. Foster, S.H. Jen, J.A. Bertrand, S.J. Cunningham, A.S. Morris, Y.C. Lee, S.M. George, M.L. Dunn, Thermo-mechanical properties of alumina films created using the atomic layer deposition technique, Sensors Actuators, A: Phys. 164 (2010) 58–67.
[49] S. Burgmann, M.J. Lid, H.J. Johnsen, N.P. Vedvik, B. Haugen, J. Provine, A.T. van Helvoort, J. Torgersen, New avenues for residual stress analysis in ultrathin atomic layer deposited free-standing membranes through release of micro-cantilevers, Heliyon 10 (2024).
[50] M. Berdova, T. Ylitalo, I. Kassamakov, J. Heino, P.T. Törmä, L. Kilpi, H. Ronkainen, J. Koskinen, E. Hæggström, S. Franssila, Mechanical assessment of suspended ALD thin films by bulge and shaft-loading techniques, Acta Mater. 66 (2014) 370–377.
[51] V. Chawla, M. Ruoho, M. Weber, A.A. Chaaya, A.A. Taylor, C. Charmette, P. Miele, M. Bechelany, J. Michler, I. Utke, Fracture mechanics and oxygen gas barrier properties of Al2O3/ZnO nanolaminates on PET deposited by atomic layer deposition, Nanomaterials 9 (2019).
[52] T. Singh, T. Lehnen, T. Leuning, D. Sahu, S. Mathur, Thickness dependence of optoelectronic properties in ALD grown ZnO thin films, Appl. Surf. Sci. 289 (2014) 27–32.